Effect of Ionospheric Variability on the Electron Energy Spectrum estimated from Incoherent Scatter Radar Measurements

Oliver Stalder[1], Björn Gustavsson[1], and Ilkka Virtanen[2]

[1]Department of Physics and Technology, University of Tromsø, Norway
[2]Space Physics and Astronomy research unit, University of Oulu, Finland

Correspondence: Oliver Stalder (ostalder@outlook.com)

Abstract. The ion composition in the E-region is modified by auroral precipitation. This affects the inversion of electron density profiles from field-aligned incoherent scatter radar measurements to differential energy spectra of precipitating electrons. Here a fully dynamic ionospheric chemistry model (IonChem) is developed that integrates the coupled continuity equations for 6 ion and 9 neutral species, modeling the rapid ionospheric variability during active aurora. IonChem is used to produce accurate, time-dependent recombination rates for ELSPEC to improve the inversion of electron density profiles to primary electron energy spectra. The improvement of the dynamic recombination rates on the inversion is compared with static recombination rates from the International Reference Ionosphere (IRI) and the steady-state recombination rates from ~~a~~ an ionospheric chemistry model, FlipChem. A systematic overestimation at high electron energies can be removed using a dynamic model. The comparison with FlipChem shows that short-timescale density variations are missed in a steady-state chemistry model.

1 Introduction

The aurora is a dynamical high-latitude ~~phenomena~~ phenomenon caused by magnetospheric electrons and protons with energies in the range of keV precipitating into the ionosphere. Precipitation leads to rapidly varying ionization, excitation and heating over a large range of spatial scales, with higher primary electron energy causing more ionization at lower heights. Precipitation also impacts the E-region substantially by inducing compositional changes and increasing conductivities. Spatial and temporal changes in ionospheric conductivities affect currents and field-aligned potentials. Precipitation can dominate power deposition at small spatial and temporal scales (e.g., Palmroth et al., 2006), and, for all these reasons, plays an important role in ~~magnetospheric-ionospheric~~ magnetosphere-ionosphere (MI) coupling. The energy spectrum of primary electrons and its time variation make it possible to investigate the acceleration process in the magnetosphere causing aurora. Understanding the dynamics of MI coupling and the ~~role of precipitation in particular are still~~ ionospheric response to rapid variation of precipitation are active research topics.

Ground-based measurements complement in-situ observations of electron precipitation. Satellites and rockets can measure the electron energy distribution directly, but their ~~trajectories~~ high velocities do not allow for extended measurements at a single location. Disentangling spatial from temporal variations can be challenging, and, for satellites, the resulting spatial resolution may be limited ~~due to the high orbital velocity. ISRs~~. Incoherent Scatter Radars (ISR) can follow the temporal evolution of

auroral precipitation above the radar's field of view for extended time periods. On the other hand, ISR measurements for this purpose are restricted to the magnetic zenith direction, and at high time resolutions one needs to adapt to high noise levels. Optical observations can complement ISR in the horizontal direction (e.g., Tuttle et al., 2014).

The electron energy spectrum can be estimated from the time-variation of E-region electron density profiles measured with ISR. The inversion starts from the electron continuity equation:

$$\frac{dn_e}{dt} + \nabla \cdot (n_e \boldsymbol{v}_e) = q_e - \bar{\alpha} n_e^2 \qquad (1)$$

where q_e is the ionization rate, $\bar{\alpha}$ the effective recombination rate and $\boldsymbol{v}_e$ is the electron drift velocity. Transport of energetic electrons along the magnetic field and ionization are governed by a set of coupled linear differential equations (e.g., Lummerzheim et al., 1989). The superposition principle applies for direct ionospheric responses such as ionization. Therefore it is possible to calculate the ionization profile as a matrix product with a discretized representation of the differential electron flux $\phi(E)$ at the top of the ionosphere:

$$q_e(z) = \boldsymbol{A} \cdot \phi(E) \qquad (2)$$

where $\boldsymbol{A}$ is the ionization-profile matrix with the ionization rates at discrete energies E and altitudes z (e.g., Fang et al., 2010; Semeter and Kamalabadi, 2005; Sergienko and Ivanov, 1993; Rees, 1989). Quantifying the ionization rate profile $q_e(z)$ makes it possible to solve for the energy spectrum $\phi(E)$. For small-scale aurora, the convection of plasma in and out of the radar beam can be significant. However, since no full-profile multi-static velocity measurements have been available, the convective term $\nabla \cdot (n_e \boldsymbol{v}_e)$ is usually neglected.

The first methods to perform this inversion estimated $q_e(z)$ from Eq. (1) assuming steady-state, i.e., that ion production and recombination are in balance at all times, e.g., UNTANGLE by Vondrak and Baron (1977) and CARD by Brekke et al. (1989). Kirkwood (1988) first considered non-steady-state conditions in the SPECTRUM algorithm, enabling reasonable estimates even when the electron precipitation varies on time-scales shorter than the recombination time, i.e., during auroral precipitation. Semeter and Kamalabadi (2005) first formulated this as a general inverse problem and used the maximum entropy method to regularize the solution. However, these direct methods run into two problems: The amplification of measurement noise when dn_e/dt and n_e^2 in Eq. (1) are taken directly from the measurements, and the ill-conditioned nature of the inverse problem from ionization profile to energy spectrum. Those are addressed with the ELSPEC method by Virtanen et al. (2018), where the electron density is modeled by integrating the continuity equation, using Eq. (2) for the production term. Thereby the explicit calculation of dn_e/dt is avoided. The inversion is recast into a non-linear minimization problem, selecting for the best energy spectrum that minimizes differences between measured and modeled electron density.

In this work we present a refined ELSPEC version, where a dynamic ionospheric composition model, IonChem, is added. IonChem integrates the continuity equation for 15 ionospheric species, capturing the full dynamics in composition even during rapidly varying auroral precipitation. This enables us to study the effects of variation in ionospheric composition and, in consequence, the effective recombination rate on the estimation of primary electron spectra from ISR data. The method we present here aims to improve the electron energy spectra estimates and to study the effects of ionospheric variation.

2 Method

This section begins with a description of ELSPEC, the method used to estimate electron energy spectra from electron density profiles. The following section describes the ion chemistry model. In section 2.3 the coupling of IonChem into ELSPEC is explained. Next, the robustness of the technique under uncertain initial compositions is analyzed. In the last section a steady-state ion chemistry model, FlipChem, is introduced, which will be used for comparison.

2.1 ELSPEC

In this study, the ELSPEC algorithm (Virtanen et al., 2018) is used for inversion, extended by a robust statistics implementation [B. Gustavsson, unpublished]. ELSPEC estimates the primary electron differential number flux $\phi(E)$ $[\text{m}^{-2}\text{s}^{-1}\text{eV}^{-1}]$ by searching for the parameterized spectrum that minimizes the corrected Akaike information criterion (cAIC). The cAIC is calculated as the residual sum-of-squares of the difference between observed (n_e^o) and modeled (n_e^m) electron density profiles during a time period, with ~~an additional~~ a cost term for the number of free parameters L that prevents overfitting for small sample sizes:

$$cAIC = \sum \frac{(n_e^o - n_e^m)^2}{\sigma_{n_e^o}^2} + \frac{2(L+1)(L+2)}{M-L} \tag{3}$$

with $\sigma_{n_e^o}^2$ being the variance in the observed electron density, and M the number of measurements. The modeled electron density is obtained by integrating Eq. (1). Allowing for a variable number of free parameters, the cAIC selects for the ~~best fitting~~ best-fitting parametrization of the electron spectrum. The robust statistics implementation starts with a coarse time interval, assuming a constant energy spectrum over 128 electron density profiles, in this case corresponding to 56 s. The time interval is recursively refined to the point where dividing an interval is not decreasing its cAIC anymore, or the time resolution imposed by the measurements is reached.

Typically an altitude-dependent, but time-constant recombination rate is used for the inversion. However, the effective recombination rate depends on the ion composition, in particular O_2^+ and NO^+, being the most abundant diatomic ions.

$$\bar{\alpha} = \alpha_{\text{NO}^+}\frac{n_{\text{NO}^+}}{n_e} + \alpha_{\text{O}_2^+}\frac{n_{\text{O}_2^+}}{n_e} \tag{4}$$

where α_{NO^+} and $\alpha_{\text{O}_2^+}$ are the recombination rates of NO^+ and O_2^+ with electrons, respectively. It has been shown that the ionospheric composition varies greatly during auroral precipitation (e.g., Jones and Rees, 1973; Zettergren et al., 2010). This impacts electron energy spectra (Virtanen et al., 2018). Newer versions of ELSPEC account for that to some extent, allowing $\bar{\alpha}$ to be calculated with FlipChem (Reimer et al., 2021), a steady-state model for ionospheric composition.

2.2 IonChem

To model the ionospheric response to the precipitation, the coupled continuity equations for electrons, ions and minor neutral species (e$^-$, H$^+$, N$^+$, O$^+$, N2$^+$, NO$^+$, O2$^+$, H, N(4S), N(2D), O(1D), O(1S), NO) are integrated in time:

$$\frac{dn_k}{dt} = q_k - l_k \tag{5}$$

where production q_k and loss l_k terms for the ion species k are of the form

$$q_k = q_{A,k} + \sum_{(i,j) \to k} \alpha_{ij} n_i n_j \tag{6}$$

$$l_k = n_k \sum_i \alpha_{ik} n_i \tag{7}$$

summed over all reactions relevant for the species k. Convection, as for electrons, is neglected. Table A1 shows the reactions, their rates α_{ij} and yields taken into account. The reaction rates are generally temperature dependent. The ion chemistry is driven by impact ionization $q_{A,k}$ of the major neutral species (Rees, 1989):

$$q_{A,O^+} = q_e \frac{0.56\, n_O}{0.92\, n_{N_2} + n_{O_2} + 0.56\, n_O} \tag{8}$$

$$q_{A,N_2^+} = q_e \frac{0.92\, n_{N_2}}{0.92\, n_{N_2} + n_{O_2} + 0.56\, n_O} \tag{9}$$

$$q_{A,O_2^+} = q_e \frac{n_{O_2}}{0.92\, n_{N_2} + n_{O_2} + 0.56\, n_O} \tag{10}$$

Density profiles of the major species (O_2, N_2, and O) are assumed to be unaffected by the precipitation. The initial composition is taken from the ~~MSIS and IRI models (Emmert et al., 2021; Bilitza et al., 2014)~~NRLMSIS2.1 and IRI-2012 models (Emmert et al., 2022; Bilitza et al., 2014), or the FlipChem model.

The reaction rates and densities span over a wide range of magnitudes. This can lead ~~solver~~ numerical ODE solvers to choose excessively small integration steps. The integration therefore may take a long time, or fails to integrate the system of coupled, non-linear, ordinary differential equations described in Eq. (5) (Nikolaeva et al., 2021). This is called a stiff problem, and a stiff solver may be used to address it. Here we use the BDF solver from the Python SciPy package.

2.3 Coupling ELSPEC and IonChem

ELSPEC solves an optimization problem for every time interval over which the energy spectrum is assumed to be fixed, evaluating the cAIC many times to find the best fitting electron spectrum. Ideally, the electron continuity equation should be integrated together with the other continuity equations, as they are coupled. However, this would be computationally expensive.

Instead, an iterative approach was ~~adapted~~adopted, illustrated in Figure 1. ELSPEC only integrates the electron continuity equation, assuming fixed recombination rates over the duration of the ~~measurements~~ measurement's time resolution. The electron continuity equation is thereby effectively decoupled from the ionospheric chemistry, simplifying the problem substantially. The resulting energy spectra $\phi^i(E)$ of the ith iteration are used to calculate the ionization rates $q_{A,k}^i$ in altitude and time. IonChem then uses these ionization rates to calculate the evolution of the minor species n_k^i and effective recombination rate $\bar{\alpha}^i$ for every measurement in altitude and time. The updated recombination rates are then used by ELSPEC in the $(i+1)^{th}$ iteration to find the optimal energy spectrum $\phi^{i+1}(E)$. When a repeated iteration over ELSPEC and IonChem converges, i.e., $\bar{\alpha}^i \approx \bar{\alpha}^{i+1}$ and $\phi^i(E) \approx \phi^{i+1}(E)$, a ~~consistent~~ solution is found.
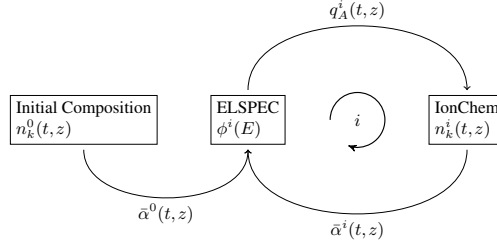
Figure 1. The iterative approach to resolve the computational challenge of pairing ELSPEC and IonChem is shown. ELSPEC is initialized with a model composition, and finds the optimal ionization rates. These are used by IonChem to find the ion densities, which then serve as the next model composition for ELSPEC. After several iterations i, the result is expected to converge.
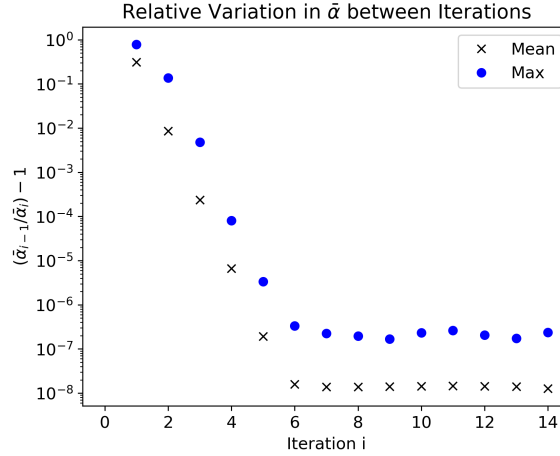
Figure 2. The relative variation in effective recombination rate between iterations $(\bar{\alpha}_{i-1} - \bar{\alpha}_i)/\bar{\alpha}_i$ shows clear convergence, both in the ~~in the~~ mean over all altitude and time bins, as well as the maximum value in all bins.

The convergence of this method is shown in Figure 2 for a test case. Over a few iterations, the effective recombination rate is converging to negligibly small deviations between iterations, measured in relative variation between iterations $(\bar{\alpha}_{i-1} - \bar{\alpha}_i)/\bar{\alpha}_i$. A relative accuracy of 10^{-7} is achieved, corresponding to the solver's relative accuracy setting.

2.4 Initial Composition

The system of coupled continuity equations is non-linear ~~, and therefore can~~and can, in principle, be sensitive to the initial conditions. In addition, the ionospheric composition can change significantly during auroral precipitation. The IRI model does
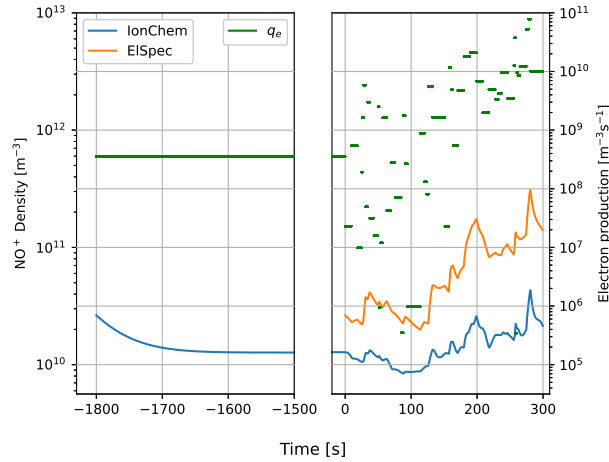
Figure 3. The effect of the 30 minute settling phase is shown on the example of NO^+ at 96 km altitude. The orange line shows the NO^+ density model used in ELSPEC, and the blue line shows the first iteration of IonChem. The green line shows the ionization rate. Before $t = 0$ s, the ionization rate is held constant, leading the IonChem composition to approach a steady-state, before the ionization rate is allowed to vary again.

not account for local auroral precipitation, it represents quiet-time conditions. IonChem therefore adds 30 minutes in front of the data set, during which a constant ionization rate is assumed, equal to that of the first ionization rate determined by ELSPEC. The model ionosphere thereby approaches a steady-state consistent with the prevalent precipitation. Figure 3 shows
125 the NO^+ density and ionization rates at 96 km altitude for the first iteration of ELSPEC and IonChem. ELSPEC starts at $t = 0$ s, integrating the continuity equation to determine the electron density. For the first iteration, ELSPEC initializes with IRI composition, i.e., the NO^+ density scales linearly with the electron density. The IonChem model starts at $t = -1800$ s, keeping the ionization rate constant for the first 30 minutes. The NO^+ density plateaus at a steady-state until $t = 0$ s, when the ionization rate varies again.
130 ~~To test the~~ For some species, such as NO or N(4S), 30 minutes will not be enough to reach steady-state. It is preferable to have a good estimate of the initial conditions, but in the limited time between auroral events, some species will never reach steady state. In a test for the implementation, IonChem was initialized with constant production rates and temperature and run until steady-state. A steady-state at constant production and without photodissociation was approached after roughly 50 hours, consistent with earlier studies (Roble and Rees, 1977; Bailey et al., 2002). Furthermore, the rapid variations during auroral
135 precipitation will cause the densities to deviate further from steady-state. The exact state of the ionosphere is not known and will not be at steady-state, making it difficult to find the exact initial conditions for IonChem. A limited time to approach a steady-state allows the densities to reach reasonable levels, placing them in the right range with the prevalent conditions.
The robustness of this approach with regard to uncertain initial conditions ~~, IonChem is run with five~~ is tested by running IonChem with different initial compositions, specified in Table 1.
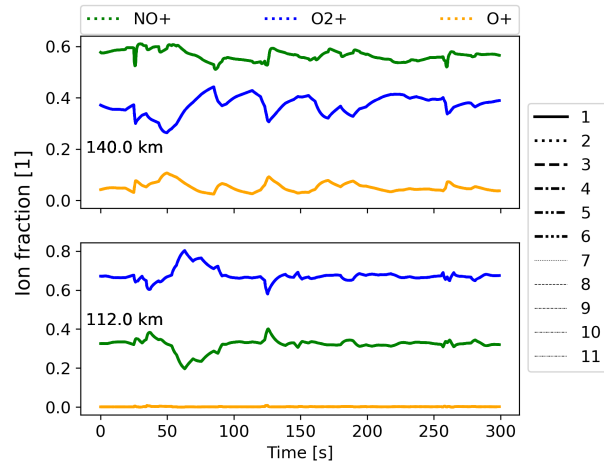
Figure 4. The integrated ion densities starting from different initial compositions are shown. The ion fractions n_k/n_e of the most important ions NO^+, O_2^+ and O^+ are plotted for 2 different altitudes. The densities coincide for all runs, ~~except for small deviations at high altitudes in case 2, where $n_{O_2^+} = n_{NO^+} = 1/2 n_e$. The solid line (case 5) shows results using IRI~~ showing that all initial conditions produce the same densities.

These test cases should cover a fairly wide range of ~~start~~ possible initial conditions, while still being reasonably close to reality. ~~All five initial ion~~ Cases 1-5 change the initial ion composition while leaving the plasma density unchanged. Cases 6-8 also change the plasma density, purposely generating a state rather far from steady-state. The effect of the NO initial density is investigated in cases 9-11.

All initial compositions produce very similar final ion composition variations. Figure 4 shows the NO^+, O_2^+ and O^+ densities for all ~~five cases. They are all coinciding, with the exception of minor deviations in case 2. We conclude that IonChem produces robust results~~ test cases. All lines are coinciding, showing that IonChem results are robust even when the initial ion composition ~~is far from the true composition.~~ unknown. Uncertain initial conditions do not seem to severely impact the solutions of this non-linear ~~system~~ problem.

2.5 FlipChem

To compare the effect of a dynamic ion chemistry model on the inversion, we use a steady-state ionospheric chemistry model FlipChem ~~(Richards et al., 2010)~~ (Reimer et al., 2021) for reference. FlipChem is a Python interface to the Ion Density Calculator, a steady-state model for ionospheric composition (Richards et al., 2010; Richards and Voglozin, 2011). It uses electron density profiles to calculate production profiles and ion densities in the lower ionosphere, under the assumption that production and losses are balanced at any time (meaning the species are in "steady-state"). It is primarily intended to calculate density variations due to slowly varying photoionisation.

FlipChem allows the ion composition to adjust to slow variations in ionization, a non-linear process due to the chemical reactions. In contrast, using IRI composition corresponds to a linear scaling of quiet-time ion densities. Still, rapid variations in ionization may cause an imbalance of production and loss terms, causing the short-timescale dynamics to be missed under steady-state assumptions. ~~Here, we use FlipChem to investigate the differences between a steady-state and a fully dynamic~~

160 ~~model. It~~

FlipChem is already implemented in newer versions of ELSPEC~~, where it calculates~~. Usually, it is used to calculate the ionospheric composition from the measured electron density in a pre-processing step. ~~To avoid FlipChem from~~

Here, we use FlipChem to investigate the differences between a steady-state and a fully dynamic ion chemistry. To avoid propagating noise from the raw electron density measurements into the ion densities, ~~ELSPEC is first run on IRI~~ in this work

165 we first run ELSPEC with IRI ion composition to produce ~~a~~ smooth electron density ~~model. This model is used instead of the raw density measurements~~ profiles, which are used to run FlipChem~~, producing smooth ion densities. The smooth FlipChem model replaces~~. The resulting, smooth FlipChem ion densities replace the IRI model in ~~the~~ a second run of ELSPEC. This corresponds to a ~~one step iteration in~~ one-step iteration with the IonChem method presented above. ~~Thereby no measurement noise of~~ This way, no noise in the electron density ~~is affecting~~ measurements affects either IonChem or FlipChem directly,

170 making for a fairer comparison between the models.

3 Results

To test this method and analyze the impact of ion composition variations on the electron energy spectra~~we look~~, we look at an event with rapid electron density variations in the E-region. Fig. 5 shows enhanced electron densities when several auroral arcs passed over the radar at about 50 s and 125 s. The data was recorded on the 12th of December 2006, 19:30-19:35

175 UT with the EISCAT UHF radar in Tromsø (Dahlgren et al., 2011). GUISDAP (Lehtinen and Huuskonen, 1996) is used to evaluate EISCAT lag profile data. A time resolution of 0.44 s in electron density is achieved, with the ISR operating in the arc1 experiment mode. At this time resolution the raw back-scattered power is used as a measure for electron density, under the assumption that electron and ion temperature are equal. The reaction rates are calculated using ion and electron temperatures estimated from the ion line spectra, integrated for 4 s to achieve an acceptable noise level. They are interpolated to match the

180 time resolution of the electron density.

The measured electron density as well as the ELSPEC electron density models based on IRI and on IonChem composition are shown in Figure 5, along with the relative variation $(n_{e,IRI} - n_{e,IC})/n_{e,IC}$. ELSPEC produces very similar electron densities with both composition models, modeling the measurements well in both cases. The differential energy flux $I_E = E\phi(E)$ produced using the IRI and IonChem models is shown in Figure 6, along with the difference $\Delta I_E = I_{E,IRI} - I_{E,IC}$ between

185 the two. ~~The difference~~ For three different slices in time, the results are also shown as a line plot, with the time marked in dashed lines in panel (c). The absolute difference (c) shows systematic negative values at the high energy tail, around 10 keV. The differences are substantial as can be seen in the line plots, with a relative correction of about 50 %. Therefore, using IonChem composition, ELSPEC produces a lower flux at high energies for all time intervals. This systematic difference is explained
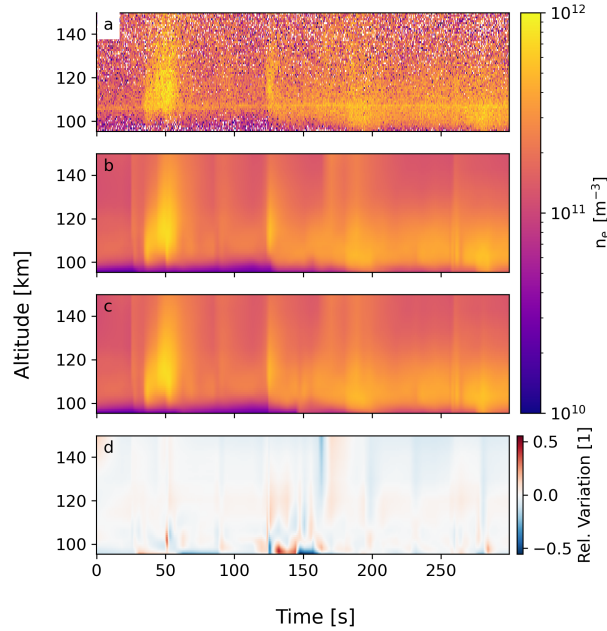
Figure 5. The measured electron density (a) is compared to the ELSPEC electron density models, using IRI composition (b) and IonChem composition (c). The measurements are reproduced well in both models. The relative variation $(n_{e,IRI} - n_{e,IC})/n_{e,IC}$ between the models in panel (d) shows that differences are small, with the biggest deviations occurring where the electron density is small.

by the ratio $r = n_{O_2^+}/n_{NO^+}$, shown in Figure 7. IonChem composition has a ~~much~~ higher ratio than IRI, especially towards
190 the lower E-region. This is expected, since IRI does not take auroral precipitation into account ~~,~~ and therefore represents quiet conditions where NO^+ is more abundant. During auroral precipitation, however, the direct production of O_2^+ makes it the dominant species at lower altitudes. Due to the lower recombination rate of O_2^+, a lower flux of primary electrons is sufficient to produce the same electron density. Using the IRI composition, representing the ionosphere at a quiet state, therefore leads to a systematic bias in the energy distribution, overestimating the energy flux at higher energies.
195   Another comparison is made with FlipChem. Being a steady-state model, it adapts to auroral precipitation, as illustrated in Figure 8 showing the O_2^+ density for both models. FlipChem predicts a large O_2^+ fraction, ~~but it~~ overestimating it above 120 km. Furthermore, it does not capture the short-timescale variation correctly. This can be seen during times of strong and rapidly varying precipitation, e.g. at 125 s in Figure 8. When IonChem models a reduction in O_2^+ fraction, FlipChem sees an increase. ~~Furthermore~~Lastly, noise in the temperature measurements ~~lead to different steady-states, propagating that~~
200 ~~noise~~ affects reaction rates, leading to different steady-state densities. The noise in temperature is thereby propagated into the FlipChem densities. ~~Due to the integration in time, IonChem is averaging out the temperature noise~~The noise in temperature is not affecting IonChem densities as much, as IonChem integrates the continuity equation dynamically. With the high time resolution (in this case 4 s for temperature), IonChem tends towards, but does not reach, steady-state in that interval, dampening the effect of noise in temperature. Furthermore, the noise in subsequent time bins has an equalizing effect.
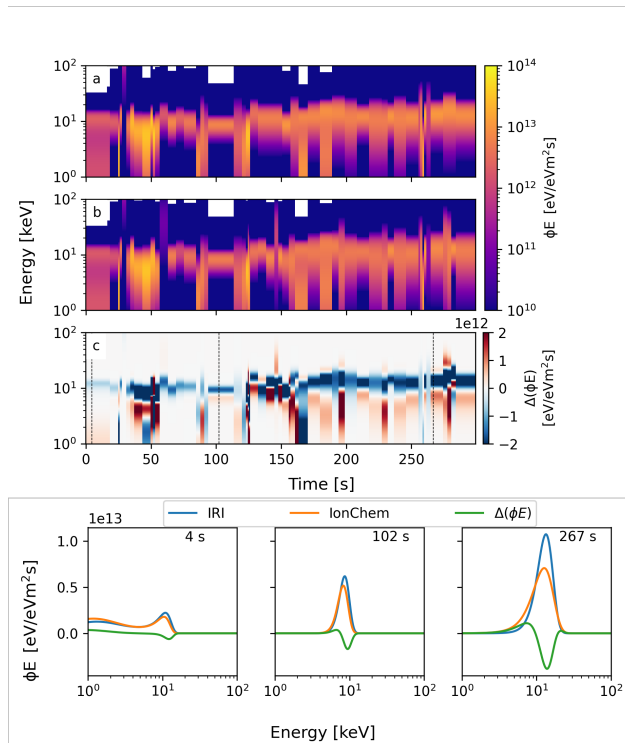
Figure 6. The energy flux spectrum using IRI composition (a) is compared to the one calculated with IonChem composition (b). Panel (c) shows the difference between the IRI and IonChem derived spectra $\Delta I_E = I_{E,IRI} - I_{E,IC}$. The three lowest panels show slices at different times. Those time slices are marked with a dashed black line in panel (c). The negative values at around 10 keV in (c) ~~shows~~ show that with the IonChem model, a lower flux at higher energies is necessary to reproduce the electron density measurements. The difference is significant, reaching up to 50 %.

The differential energy fluxes produced using FlipChem and IonChem are compared in Fig. 9. Again, a systematic shift of the flux at 10 keV - 20 keV to slightly lower energies can be seen ~~throughout all time bins~~ at all time-steps, due to the higher O_2^+ fraction at heights below 100 km in the IonChem model (see Figure 8). Furthermore, between 30 s - 70 s into the event, the flux at intermediate energies of 3 keV - 9 keV ~~is increased~~ increases, due to the decreased O_2^+ fraction.

The difference in O_2^+ fraction between the two models during strong precipitation has been investigated further, as the decrease seen in IonChem during intense precipitation might ~~at first seem counterintuitive~~ seem counterintuitive at first. Since O_2^+ is produced directly by impact ionization, one might also expect its mixing ratio to increase. Instead, we find the O_2^+ fraction temporarily decreasing, while NO^+ and O^+ fractions are increasing, as shown in Figure 10.

To study why the NO^+ fraction increases, while O_2^+ decreases, a simulation with constant, strong precipitation is run. IonChem is initialized with the densities found just before 125 s in Figure 10, and the precipitation is set to what we find at 125 s. Both O_2^+ and NO^+ densities rise, as shown in Figure 11. ~~While remains the dominant species,~~ NO^+ has a faster
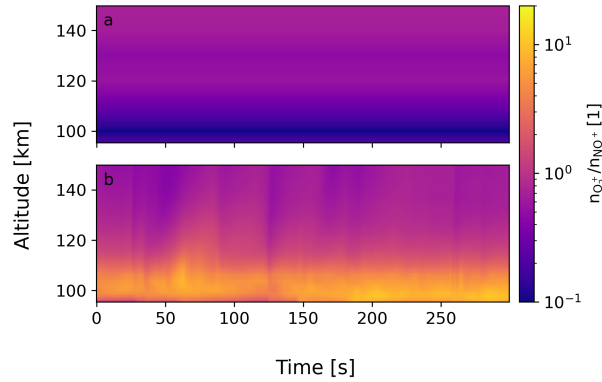
Figure 7. The ratio $r = n_{\mathrm{O}_2^+}/n_{\mathrm{NO}^+}$ is shown for (a) IRI composition and (b) IonChem composition. ~~The reversal in the~~ IonChem produces a much higher ratio at low altitudes, and also transient elevated ratios at higher altitudes. This change in $n_{\mathrm{O}_2^+}/n_{\mathrm{NO}^+}$ ratio implies differences in the effective recombination rate.
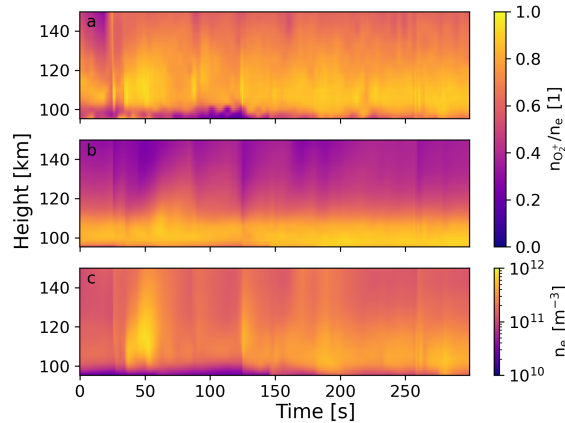
Figure 8. The top panel (a) shows the O_2^+ fraction produced by FlipChem, the middle panel (b) shows the IonChem model, and the lowest panel (c) shows the electron density for context, retrieved from the IonChem model. The noise in temperature is propagated to the fractions in the FlipChem, causing the patches in the uppermost panel.

initial growth rate, which lowers the $\mathrm{O}_2^+/\mathrm{NO}^+$ ratio, before it recovers. Having a higher recombination rate, NO^+ tends to the steady-state quicker than O_2^+. Furthermore, as atomic oxygen becomes more abundant with height, N_2^+ predominantly reacts with atomic oxygen producing NO^+ (Ulich et al., 2000). ~~The large~~ Th reaction rate enables the NO^+ fraction to increase rapidly. This causes NO^+ to become more abundant at high altitudes. After a period of high steady ionization a steady-state with an increased $\mathrm{O}_2^+/\mathrm{NO}^+$ mixing ratio is approached again.

220
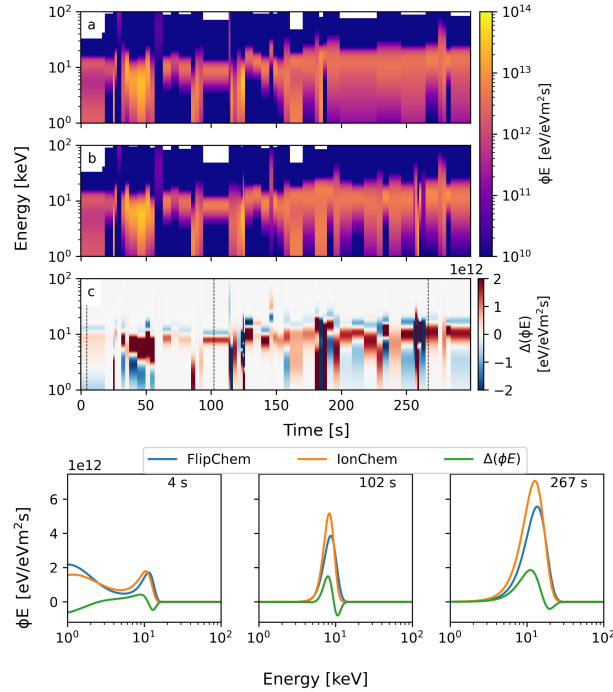
Figure 9. The energy flux spectrum using FlipChem composition (a) is compared to the one calculated with IonChem composition (b). Panel (c) shows the difference between the FlipChem and IonChem derived spectra $\Delta I_E = I_{E,FC} - I_{E,IC}$. The three lowest panels show a slice at different times. A systematic downshift from the highest energies (around 10 keV) in each timestep can be seen. Additionally, e.g., at around 50 seconds, the intermediate energies around 5 keV are enhanced.

Lastly, we find a significant O^+ fraction down to ~~110 km~~ 120 km during strong precipitation, impacting the mean ion mass (Figure 10). This has consequences in fitting the electron and ion temperatures in ISR measurements, as they depend on the mean ion mass. Fitting the temperatures and mean ion mass simultaneously is difficult (e.g., Waldteufel, 1971), therefore, a model for the ion mass is commonly used. Even though the surges are short-lived, they may affect~~for example~~, for example, high-resolution analysis as in Tesfaw et al. (2022).

4   Discussion

A new method to improve the inversion of electron density profiles to primary electron spectra is presented, that couples ~~a~~ the fully dynamic ionospheric ~~model~~ chemistry model IonChem with the time-dependent inversion algorithm ELSPEC. The iterative approach to ~~obtain simultaneously~~ simultaneously obtain electron energy spectra and ion compositions used here shows good results. It converges over a few iterations and is robust against uncertain initial conditions. The importance of using a dynamic model is shown with an example of transient effects in the O_2^+/NO^+ ratio and the O^+ fraction.
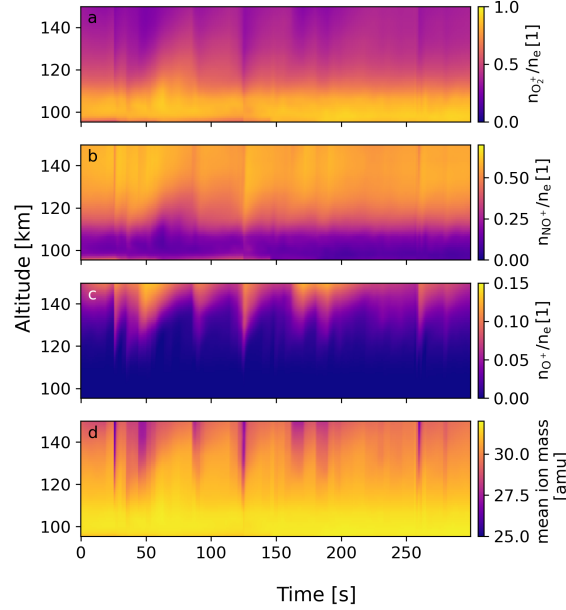
Figure 10. The fractions of O_2^+ (a), NO^+ (b) and O^+ (c) ~~show that is dominating during entire time of precipitation, especially at lower heights~~are shown. ~~However, when the~~ When precipitation spikes, we find enhancements in the mixing ratio of NO^+ and O^+. Furthermore, significant O^+ densities down to 110 km are found. This has an effect on the mean ion mass shown in (d).
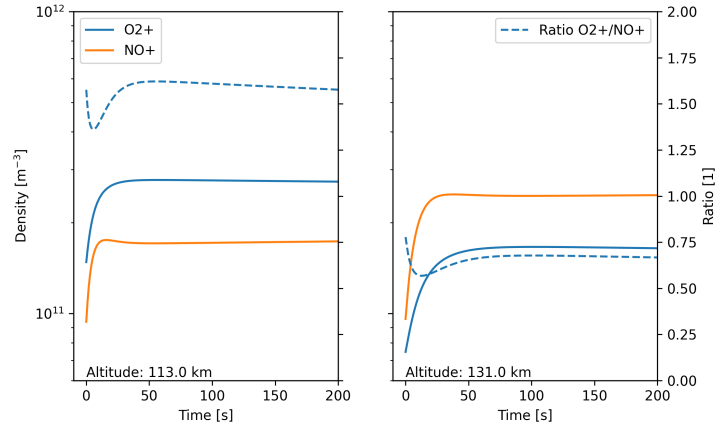
Figure 11. The evolution of O_2^+ and NO^+ densities during strong precipitation is shown at ~~140 km altitude~~two altitudes. ~~While remains the dominating species,~~ In both cases NO^+ tends quicker towards a steady-state, decreasing the O_2^+/NO^+ ratio temporarily. At lower heights, O_2^+ remains the dominating species.

ELSPEC presents an improvement compared to steady-state inversion procedures (Vondrak and Baron, 1977; Brekke et al., 1989; Miyoshi et al., 2015; Kaeppler et al., 2015), as it integrates the electron continuity equation numerically without assuming balanced ionization and recombination rate at all times. ~~Other authors used a time-dependent inversion~~ Time-dependent inversion algorithms have been used, but assumed time-constant recombination rates (Kirkwood, 1988; Semeter and Kamalabadi, 2005). ELSPEC integrates the electron continuity equation instead of using it to explicitly calculate ionization profiles, similar to Dahlgren et al. (2011). This reduces the impact of measurement noise. Here, ELSPEC ~~adjusts~~ and IonChem adjust the ion composition iteratively, while Dahlgren et al. (2011) used the Southampton ion-chemistry model to calculate the ion densities once, corresponding to one iteration. A similar method is used by Turunen et al. (2016), where the Sodankylä ~~Ion and neutral~~ Ion-Neutral Chemistry model (SIC) is employed. The ~~best fitting~~ best-fitting ionization profile is ~~determined~~ found iteratively by integrating the coupled continuity equations of electrons and ions. The energy spectrum is then calculated using the CARD method, assuming steady-state conditions.

The method presented here is a tool that can help to improve studies of auroral precipitation, such as Tesfaw et al. (2023), and will be of interest for research with EISCAT_3D radar (McCrea et al., 2015). ELSPEC can be used to provide additional insight in conjunction with other observations, complementing the field-aligned ISR measurements~~for example~~, for example, with optical measurements in the horizontal direction (Wedlund et al., 2013; Tuttle et al., 2014) or satellite conjunctions (Kirkwood and Eliasson, 1990).

Further improvements to the IonChem model could be made by taking production of excited states and spontaneous emissions into account; photoionization can be added to make it compatible with daylight conditions. With EISCAT_~~3D enabling~~ 3Ds capability for volumetric measurements of both electron densities and plasma drifts~~should make it~~, it should be possible to account for convection. Diffusion of neutral and ion species can be taken into account, in particular to account for transport of NO (Bailey et al., 2002). Plasmaline measurements already allow for more precise determination of electron density profiles today, see Vierinen et al. (2016). They should become routinely available with the higher sensitivity of EISCAT_3D.

5 Conclusion

Improved estimates of electron energy spectra from electron density profiles can be made by combining a dynamical ion chemistry model (IonChem) with the ELSPEC algorithm. The improvement of the dynamical chemistry is that it captures the variation of the ion composition during periods of rapidly changing precipitation. We find a systematic reduction of the electron fluxes at higher energies, in our test case at around 10 keV, resulting from a dynamical variation of the ion composition. The cause of this reduction is due to the variability of the O_2^+ to NO^+ mixing ratio. We have also made a comparison between our dynamical chemistry and a steady-state chemistry, FlipChem. The results show that variations in ion composition during rapid variations of ionization captured by the dynamical chemistry ~~is~~ are not captured by a steady-state model. A rapid increase of ionization rate leads to a faster transient response of NO^+ compared to O_2^+ density. Also here, a systematic reduction of the high energy tail is found when using a dynamic model, albeit to a lesser extend. Overall, modeling the ionospheric composition improves the quality of the inversion from electron density profiles to energy spectra.

265 *Code and data availability.* IonChem is an open-source software, that is easily extended with more reactions. All code is available on Github: https://github.com/ostald/juliaIC.

ELSPEC is available on GitHub: https://github.com/ilkkavir/ELSPEC. The robust statistics fork used here can be found on https://github.com/ostald/ELSPEC/tree/recursive.

EISCAT data supporting this research can be found in the EISCAT archives: https://portal.eiscat.se/schedule

Reaction	Rate $[\mathrm{m^3s^{-1}}]$	Branching ratio	Source
$N^+ + NO \rightarrow N_2^+ + O$	$8.33 \times 10^{-17}(300/T_i)^{0.24}$		Richards
$N^+ + NO \rightarrow NO^+ + N(4S)$	$4.72 \times 10^{-16}(300/T_i)^{0.24}$		Richards
$N^+ + O \rightarrow O^+(4S) + N(4S)$	2.2×10^{-18}		Richards
$N^+ + O_2 \rightarrow NO^+ + O(1D)$	$0.36 \begin{cases} 5.5 \times 10^{-16}(T_i/300)^{0.45} & T_i \leq 1000 \\ 9.5 \times 10^{-16} & T_i > 1000 \end{cases}$		Richards
$N^+ + O_2 \rightarrow NO^+ + O$	$0.09 \begin{cases} 5.5 \times 10^{-16}(T_i/300)^{0.45} & T_i \leq 1000 \\ 9.5 \times 10^{-16} & T_i > 1000 \end{cases}$		Richards
$N^+ + O_2 \rightarrow O^+(4S) + NO$	$0.05 \begin{cases} 5.5 \times 10^{-16}(T_i/300)^{0.45} & T_i \leq 1000 \\ 9.5 \times 10^{-16} & T_i > 1000 \end{cases}$		Richards
$N^+ + O_2 \rightarrow O_2^+ + N(2D)$	$0.15 \begin{cases} 5.5 \times 10^{-16}(T_i/300)^{0.45} & T_i \leq 1000 \\ 9.5 \times 10^{-16} & T_i > 1000 \end{cases}$		Richards
$N^+ + O_2 \rightarrow O_2^+ + N(4S)$	$0.35 \begin{cases} 5.5 \times 10^{-16}(T_i/300)^{0.45} & T_i \leq 1000 \\ 9.5 \times 10^{-16} & T_i > 1000 \end{cases}$		Richards
$N^+ + H \rightarrow H^+ + N(4S)$	3.6×10^{-18}		Rees
$N_2^+ + e^- \rightarrow N(4S)$	$2.2 \times 10^{-13}(300/T_e)^{0.39}$	2	Richards
$N_2^+ + N(4S) \rightarrow N_2 + N^+$	1.0×10^{-17}		Richards
$N_2^+ + NO \rightarrow N_2 + NO^+$	3.6×10^{-16}		Richards
$N_2^+ + O \rightarrow NO^+ + N(4S)$	$1.33 \times 10^{-16}(300/T_i)^{0.44}$		Richards
$N_2^+ + O \rightarrow O^+(4S) + N_2$	$7.0 \times 10^{-18}(300/T_i)^{0.23}$		Richards
$N_2^+ + O_2 \rightarrow O_2^+ + N_2$	$\begin{cases} 5.1 \times 10^{-17}(300/T_i)^{1.16} & T_i \leq 1000 \\ 1.26 \times 10^{-17}(T_i/1000)^{0.67} & T_i > 1000 \end{cases}$		Richards
$NO^+ + e^- \rightarrow N(2D) + O$	$3.4 \times 10^{-13}(300/T_e)^{0.85}$		Richards
$NO^+ + e^- \rightarrow N(4S) + O$	$0.6 \times 10^{-13}(300/T_e)^{0.85}$		Richards
$O^+(4S) + H \rightarrow O + H^+$	6.4×10^{-16}		Richards
$O^+(4S) + N(2D) \rightarrow N^+ + O$	1.3×10^{-16}		Richards
$O^+(4S) + N_2 \rightarrow NO^+ + N(4S)$	$\begin{cases} 1.2 \times 10^{-18}(300/T_i)^{0.45} & T_i \leq 1000 \\ 7.0 \times 10^{-19}(T_i/1000)^{2.12} & T_i > 1000 \end{cases}$		Richards

Reaction	Rate		Reference
$O^+(4S) + NO \rightarrow NO^+ + O$	$7.0 \times 10^{-19} (300/T_i)^{-0.87}$		Richard
$O^+(4S) + O_2 \rightarrow O_2^+ + O$	$\begin{cases} 1.6 \times 10^{-17} (300/T_i)^{0.52} & T_i \leq 900 \\ 9.0 \times 10^{-18} (T_i/900)^{0.92} & T_i > 900 \end{cases}$		Richards
$O_2^+ + e^- \rightarrow O$	$\begin{cases} 1.95 \times 10^{-13} (300/T_e)^{0.70} & T_i \leq 1200 \\ 7.39 \times 10^{-14} (1200/T_e)^{0.56} & T_i > 1200 \end{cases}$	2	Richards
$O_2^+ + N(2D) \rightarrow NO^+ + O$	1.8×10^{-16}		Richards
$O_2^+ + N(2D) \rightarrow N^+ + O_2$	8.65×10^{-17}		Richards
$O_2^+ + N(2P) \rightarrow N(4S) + O_2^+$	2.2×10^{-17}		Richards
$O_2^+ + N(4S) \rightarrow NO^+ + O$	1.0×10^{-16}		Richards
$O_2^+ + NO \rightarrow NO^+ + O_2$	4.5×10^{-16}		Richards
$O_2^+ + N_2 \rightarrow NO^+ + NO$	5.0×10^{-22}		Rees
$O^+(2D) + e^- \rightarrow O^+(4S) + e^-$	$6.03 \times 10^{-14} (300/T_e)^{0.5}$		Richards
$O^+(2D) + N(4S) \rightarrow N^+ + O$	1.5×10^{-16}		Richards
$O^+(2D) + N_2 \rightarrow N_2^+ + O$	$1.5 \times 10^{-16} (300/T_i)^{-0.55}$		Richards
$O^+(2D) + N_2 \rightarrow NO^+ + N(4S)$	2.5×10^{-17}		Richards
$O^+(2D) + N_2 \rightarrow O^+(4S) + N_2$	8.0×10^{-16}		Rees
$O^+(2D) + NO \rightarrow NO^+ + O$	1.2×10^{-15}		Richards
$O^+(2D) + O \rightarrow O^+(4S) + O$	1.0×10^{-17}		Richards
$O^+(2D) + O_2 \rightarrow O_2^+ + O$	7.0×10^{-16}		Richards
$O^+(2P) + e^- \rightarrow O^+(2D) + e^-$	$1.84 \times 10^{-13} (300/T_e)^{0.5}$		Richards
$O^+(2P) + e^- \rightarrow O^+(4S) + e^-$	$3.03 \times 10^{-14} (300/T_e)^{0.5}$		Richards
$O^+(2P) + N_2 \rightarrow N_2^+ + O$	$2.0 \times 10^{-16} (300/T_i)^{-0.55}$		Richards
$O^+(2P) + N_2 \rightarrow N^+ + NO$	1.0×10^{-16}		Rees
$O^+(2P) + O \rightarrow O^+(4S) + O$	4.0×10^{-16}		Richards
$O^+(2P) + O_2 \rightarrow O^+(4S) + O_2$	1.3×10^{-16}		Richards
$O^+(2P) + O_2 \rightarrow O_2^+ + O$	1.3×10^{-16}		Richards
$O^+(2P) + N(4S) \rightarrow N^+ + O$	1.0×10^{-16}		Rees
$N(4S) + O_2 \rightarrow NO + O$	$4.4 \times 10^{-18} \exp(-3220/T_n)$		Rees
$N(4S) + NO \rightarrow N_2 + O$	$1.5 \times 10^{-18} T_n^{0.50}$		Rees
$N(2D) + O_2 \rightarrow NO + O(1D) + O$	5.3×10^{-18}	1.00, 0.10, 0.90	Rees
$N(2D) + O \rightarrow N(4S) + O$	2.0×10^{-18}		Rees
$N(2D) + e^- \rightarrow N(4S) + e^-$	$5.5 \times 10^{-16} (T_e/300)^{0.5}$		Rees
$N(2D) + NO \rightarrow N_2 + O$	7.0×10^{-17}		Rees
$H^+ + O \rightarrow O^+(4S) + H$	$(8/9)6.0 \times 10^{-16} \sqrt{(T_i + (T_n/4)/(T_n + (T_i/16)}$		Rees

Table A1: Chemical reactions in the E-region and reaction rates, as well as branching ratios for reactions with several possible products. From Richards and Voglozin (2011) and Rees (1989).

Author contributions. OS wrote the IonChem algorithm and its integration into ELSPEC. BG and IV wrote the ELSPEC algorithm on which this work builds. Both were contributing to this project through numerous discussions and ideas. OS prepared the manuscript, with contrition from both co-authors.

275 *Competing interests.* The authors declare that they have no conflict of interest.

Acknowledgements. EISCAT was an international association supported by research organisations in China (CRIRP), Finland (SA), Japan (NIPR and ISEE), Norway (NFR), Sweden (VR), and the United Kingdom (UKRI). EISCAT AB is now the successor.

References

Bailey, S. M., Barth, C. A., and Solomon, S. C.: A model of nitric oxide in the lower thermosphere, Journal of Geophysical Research: Space Physics, 107, SIA 22–1–SIA 22–12, https://doi.org/10.1029/2001JA000258, _eprint: https://agupubs.onlinelibrary.wiley.com/doi/pdf/10.1029/2001JA000258, 2002.

Bilitza, D., Altadill, D., Zhang, Y., Mertens, C., Truhlik, V., Richards, P., McKinnell, L.-A., and Reinisch, B.: The International Reference Ionosphere 2012 – a model of international collaboration, Journal of Space Weather and Space Climate, 4, A07, https://doi.org/10.1051/swsc/2014004, publisher: EDP Sciences, 2014.

Brekke, A., Hall, C., and Hansen, T. L.: Auroral ionospheric conductances during disturbed conditions, Annales Geophysicae, 7, 269–280, https://ui.adsabs.harvard.edu/abs/1989AnGeo...7..269B, aDS Bibcode: 1989AnGeo...7..269B, 1989.

Dahlgren, H., Gustavsson, B., Lanchester, B. S., Ivchenko, N., Brändström, U., Whiter, D. K., Sergienko, T., Sandahl, I., and Marklund, G.: Energy and flux variations across thin auroral arcs, Annales Geophysicae, 29, 1699–1712, https://doi.org/10.5194/angeo-29-1699-2011, publisher: Copernicus GmbH, 2011.

Emmert, J. T., Drob, D. P., Picone, J. M., Siskind, D. E., Jones Jr., M., Mlynczak, M. G., Bernath, P. F., Chu, X., Doornbos, E., Funke, B., Goncharenko, L. P., Hervig, M. E., Schwartz, M. J., Sheese, P. E., Vargas, F., Williams, B. P., and Yuan, T.: NRLMSIS 2.0: A Whole-Atmosphere Empirical Model of Temperature and Neutral Species Densities, Earth and Space Science, 8, e2020EA001321, https://doi.org/10.1029/2020EA001321, _eprint: https://onlinelibrary.wiley.com/doi/pdf/10.1029/2020EA001321, 2021.

Emmert, J. T., Jones Jr, M., Siskind, D. E., Drob, D. P., Picone, J. M., Stevens, M. H., Bailey, S. M., Bender, S., Bernath, P. F., Funke, B., Hervig, M. E., and Pérot, K.: NRLMSIS 2.1: An Empirical Model of Nitric Oxide Incorporated Into MSIS, Journal of Geophysical Research: Space Physics, 127, e2022JA030896, https://doi.org/10.1029/2022JA030896, _eprint: https://agupubs.onlinelibrary.wiley.com/doi/pdf/10.1029/2022JA030896, 2022.

Fang, X., Randall, C. E., Lummerzheim, D., Wang, W., Lu, G., Solomon, S. C., and Frahm, R. A.: Parameterization of monoenergetic electron impact ionization, Geophysical Research Letters, 37, https://doi.org/10.1029/2010GL045406, _eprint: https://onlinelibrary.wiley.com/doi/pdf/10.1029/2010GL045406, 2010.

Jones, R. A. and Rees, M. H.: Time dependent studies of the aurora—I. Ion density and composition, Planetary and Space Science, 21, 537–557, https://doi.org/10.1016/0032-0633(73)90069-X, 1973.

Kaeppler, S. R., Hampton, D. L., Nicolls, M. J., Strømme, A., Solomon, S. C., Hecht, J. H., and Conde, M. G.: An investigation comparing ground-based techniques that quantify auroral electron flux and conductance, Journal of Geophysical Research: Space Physics, 120, 9038–9056, https://doi.org/10.1002/2015JA021396, _eprint: https://onlinelibrary.wiley.com/doi/pdf/10.1002/2015JA021396, 2015.

Kirkwood, S.: SPECTRUM: A computer algorithm to derive the flux-energy spectrum of precipitating particles from EISCAT electron density profiles, Tech. rep., https://ui.adsabs.harvard.edu/abs/1988scad.rept.....K, publication Title: Unknown ADS Bibcode: 1988scad.rept.....K, 1988.

Kirkwood, S. and Eliasson, L.: Energetic particle precipitation in the substorm growth phase measured by EISCAT and Viking, Journal of Geophysical Research: Space Physics, 95, 6025–6037, https://doi.org/10.1029/JA095iA05p06025, _eprint: https://onlinelibrary.wiley.com/doi/pdf/10.1029/JA095iA05p06025, 1990.

Lehtinen, M. S. and Huuskonen, A.: General incoherent scatter analysis and GUISDAP, Journal of Atmospheric and Terrestrial Physics, 58, 435–452, https://doi.org/10.1016/0021-9169(95)00047-X, 1996.

Lummerzheim, D., Rees, M. H., and Anderson, H. R.: Angular dependent transport of auroral electrons in the upper atmosphere, Planetary and Space Science, 37, 109–129, https://doi.org/10.1016/0032-0633(89)90074-3, 1989.

McCrea, I., Aikio, A., Alfonsi, L., Belova, E., Buchert, S., Clilverd, M., Engler, N., Gustavsson, B., Heinselman, C., Kero, J., Kosch, M., Lamy, H., Leyser, T., Ogawa, Y., Oksavik, K., Pellinen-Wannberg, A., Pitout, F., Rapp, M., Stanislawska, I., and Vierinen, J.: The science case for the EISCAT_3D radar, Progress in Earth and Planetary Science, 2, 21, https://doi.org/10.1186/s40645-015-0051-8, 2015.

Miyoshi, Y., Oyama, S., Saito, S., Kurita, S., Fujiwara, H., Kataoka, R., Ebihara, Y., Kletzing, C., Reeves, G., Santolik, O., Clilverd, M., Rodger, C. J., Turunen, E., and Tsuchiya, F.: Energetic electron precipitation associated with pulsating aurora: EISCAT and Van Allen Probe observations, Journal of Geophysical Research: Space Physics, 120, 2754–2766, https://doi.org/10.1002/2014JA020690, _eprint: https://onlinelibrary.wiley.com/doi/pdf/10.1002/2014JA020690, 2015.

Nikolaeva, V., Gordeev, E., Sergienko, T., Makarova, L., and Kotikov, A.: AIM-E: E-Region Auroral Ionosphere Model, Atmosphere, 12, 748, https://doi.org/10.3390/atmos12060748, number: 6 Publisher: Multidisciplinary Digital Publishing Institute, 2021.

Palmroth, M., Janhunen, P., Germany, G., Lummerzheim, D., Liou, K., Baker, D. N., Barth, C., Weatherwax, A. T., and Watermann, J.: Precipitation and total power consumption in the ionosphere: Global MHD simulation results compared with Polar and SNOE observations, Annales Geophysicae, 24, 861–872, https://doi.org/10.5194/angeo-24-861-2006, publisher: Copernicus GmbH, 2006.

Rees, M. H.: Physics and Chemistry of the Upper Atmosphere, Cambridge Atmospheric and Space Science Series, Cambridge University Press, Cambridge, ISBN 978-0-521-36848-3, https://doi.org/10.1017/CBO9780511573118, 1989.

Reimer, A., amisr user, and FGuenzkofer: amisr/flipchem: v2021.2.2 Bugfix Release, https://doi.org/10.5281/zenodo.5719844, 2021.

Richards, P. G. and Voglozin, D.: Reexamination of ionospheric photochemistry, Journal of Geophysical Research: Space Physics, 116, https://doi.org/10.1029/2011JA016613, _eprint: https://onlinelibrary.wiley.com/doi/pdf/10.1029/2011JA016613, 2011.

Richards, P. G., Bilitza, D., and Voglozin, D.: Ion density calculator (IDC): A new efficient model of ionospheric ion densities, Radio Science, 45, https://doi.org/10.1029/2009RS004332, _eprint: https://onlinelibrary.wiley.com/doi/pdf/10.1029/2009RS004332, 2010.

Roble, R. G. and Rees, M. H.: Time-dependent studies of the aurora: Effects of particle precipitation on the dynamic morphology of ionospheric and atmospheric properties, Planetary and Space Science, 25, 991–1010, https://doi.org/10.1016/0032-0633(77)90146-5, 1977.

Semeter, J. and Kamalabadi, F.: Determination of primary electron spectra from incoherent scatter radar measurements of the auroral E region, Radio Science, 40, https://doi.org/10.1029/2004RS003042, _eprint: https://onlinelibrary.wiley.com/doi/pdf/10.1029/2004RS003042, 2005.

Sergienko, T. and Ivanov, V.: A new approach to calculate the excitation of atmospheric gases by auroral electrons, Annales Geophysicae, 11, 717–727, 1993.

Tesfaw, H. W., Virtanen, I. I., Aikio, A. T., Nel, A., Kosch, M., and Ogawa, Y.: Precipitating Electron Energy Spectra and Auroral Power Estimation by Incoherent Scatter Radar With High Temporal Resolution, Journal of Geophysical Research: Space Physics, 127, e2021JA029 880, https://doi.org/10.1029/2021JA029880, _eprint: https://onlinelibrary.wiley.com/doi/pdf/10.1029/2021JA029880, 2022.

Tesfaw, H. W., Virtanen, I. I., and Aikio, A. T.: Characteristics of Auroral Electron Precipitation at Geomagnetic Latitude 67° Over Tromsø, Journal of Geophysical Research: Space Physics, 128, e2023JA031 382, https://doi.org/10.1029/2023JA031382, _eprint: https://onlinelibrary.wiley.com/doi/pdf/10.1029/2023JA031382, 2023.

Turunen, E., Kero, A., Verronen, P. T., Miyoshi, Y., Oyama, S.-I., and Saito, S.: Mesospheric ozone destruction by high-energy electron precipitation associated with pulsating aurora, Journal of Geophysical Research: Atmospheres, 121, 11,852–11,861, https://doi.org/10.1002/2016JD025015, _eprint: https://onlinelibrary.wiley.com/doi/pdf/10.1002/2016JD025015, 2016.

Tuttle, S., Gustavsson, B., and Lanchester, B.: Temporal and spatial evolution of auroral electron energy spectra in a region surrounding the magnetic zenith, Journal of Geophysical Research: Space Physics, 119, 2318–2327, https://doi.org/10.1002/2013JA019627, _eprint: https://onlinelibrary.wiley.com/doi/pdf/10.1002/2013JA019627, 2014.

Ulich, T., Turunen, E., and Nygrén, T.: Effective recombination coefficient in the lower ionosphere during bursts of auroral electrons, Advances in Space Research, 25, 47–50, https://doi.org/10.1016/S0273-1177(99)00896-0, 2000.

Vierinen, J., Bhatt, A., Hirsch, M. A., Strømme, A., Semeter, J. L., Zhang, S.-R., and Erickson, P. J.: High temporal resolution observations of auroral electron density using superthermal electron enhancement of Langmuir waves, Geophysical Research Letters, 43, 5979–5987, https://doi.org/10.1002/2016GL069283, _eprint: https://onlinelibrary.wiley.com/doi/pdf/10.1002/2016GL069283, 2016.

Virtanen, I. I., Gustavsson, B., Aikio, A., Kero, A., Asamura, K., and Ogawa, Y.: Electron Energy Spectrum and Auroral Power Estimation From Incoherent Scatter Radar Measurements, Journal of Geophysical Research: Space Physics, 123, 6865–6887, https://doi.org/10.1029/2018JA025636, _eprint: https://onlinelibrary.wiley.com/doi/pdf/10.1029/2018JA025636, 2018.

Vondrak, R. and Baron, M.: A method of obtaining the energy distribution of auroral electrons from incoherent scatter radar measurements, Universitetsforlaget, Norway, iNIS Reference Number: 11499528, 1977.

Waldteufel, P.: Combined incoherent-scatter F 1-region observations, Journal of Geophysical Research (1896-1977), 76, 6995–6999, https://doi.org/10.1029/JA076i028p06995, _eprint: https://onlinelibrary.wiley.com/doi/pdf/10.1029/JA076i028p06995, 1971.

Wedlund, C. S., Lamy, H., Gustavsson, B., Sergienko, T., and Brändström, U.: Estimating energy spectra of electron precipitation above auroral arcs from ground-based observations with radar and optics, Journal of Geophysical Research: Space Physics, 118, 3672–3691, https://doi.org/10.1002/jgra.50347, _eprint: https://onlinelibrary.wiley.com/doi/pdf/10.1002/jgra.50347, 2013.

Zettergren, M., Semeter, J., Burnett, B., Oliver, W., Heinselman, C., Blelly, P.-L., and Diaz, M.: Dynamic variability in F-region ionospheric composition at auroral arc boundaries, Annales Geophysicae, 28, 651–664, https://doi.org/10.5194/angeo-28-651-2010, publisher: Copernicus GmbH, 2010.

Table 1. Start conditions

Case	Initial Composition	Comments
1	IRI-2012, NRLMSIS2.1 composition	Reference for comparison.
2	Swapping O_2^+ and NO^+ densities compared to IRI composition.	During intense precipitation, the directly produced O_2^+ densities may surpass NO^+ levels.
~~2~~ 3	$n_{O_2^+} = n_{NO^+} = 1/2\, n_e$	Starting with O_2^+ and NO^+ ions in equal amounts at all altitudes
~~3~~ 4	$n_{O_2^+}$ = ~~3/10 n_e~~ $2\,n_{O^+,IRI}$ n_{O^+} n_{NO^+} = ~~3/10 n_e~~ n_e $\sum n_{ions}$ n_{O^+}	An increased fraction of O^+ is assumed due to ongoing precipitation. The densities of the other ions are re-scaled to maintain the plasma density.
5	$n_{O_2^+}$ = ~~3/10 n_e~~ $1.5\,n_{O_2^+,IRI}$ $n_{N_2^+}$ = ~~1/10 n_e~~ n_e $\sum n_{ions}$	~~Presence of O^+ and N_2^+~~ An increased fraction of O_2^+ is assumed due to ongoing precipitation. ~~Having a large loss rate, the density of N_2^+ is purposely overestimated~~ The densities of the other ions are re-scaled to maintain the plasma density.
~~4~~ 6	$n_{O_2^+}$ = ~~1/10 n_e~~ $2\,n_{O_2^+,IRI}$ n_{NO^+} = ~~3/10 n_e~~ $\sum n_{ions}$ n_e n_{O^+}	An increased O_2^+ density is assumed due to ongoing precipitation. The plasma density is increased by the additional ion density.
7	n_i = ~~6/10 n_e~~ $2\,n_{i,IRI}$ n_e = $\sum n_{ions}$	~~A large fraction of O^+ ions is assumed, reflecting the large production at higher altitudes during auroral active periods~~ All ion densities are increased. The plasma density is increased by the additional ion density.
8	$n_{N_2^+}$ = $0.002\,n_{O^+}$ n_e = $\sum n_{ions}$	The starting density of $n_{N_2^+}$ is set to be non-zero. The plasma density is increased by the additional ion density.
~~5~~ 9	~~IRI composition~~ n_{NO} = ~~Reference for comparison~~ $10\,n_{NO,NRLMSIS2.1}$	Increased NO density is assumed due to ongoing precipitation.
10	n_{NO} = $100\,n_{NO,NRLMSIS2.1}$	Increased NO density is assumed due to ongoing precipitation.
11	n_{NO} = 0	No NO density for comparison with earlier MSIS models.